AIMS Materials Science, 13(5): 913–938.
DOI: 10.3934/matersci.2026043
Received: 18 August 2026
Revised: 07 September 2026
Accepted: 22 September 2026
Published: 15 October 2026

https://www.aimspress.com/journal/Materials

Research article

Glass-phase microstructure and He/Ne separation performance of cenosphere-based microspherical membranes

Elena V. Fomenko[1,*], Timur Yu. Ivanenko[1], Sergey V. Kukhtetskiy[1], Nikolay P. Shestakov[2], Alexander S. Krylov[2], Leonid A. Solovyov[1] and Tatiana A. Vereshchagina[1]

[1] Institute of Chemistry and Chemical Technology, Federal Research Center, Krasnoyarsk Science Center of the Siberian Branch of the Russian Academy of Sciences, Akademgorodok 50/24, 660036 Krasnoyarsk, Russia

[2] L.V. Kirensky Institute of Physics, Federal Research Center, Krasnoyarsk Science Center of the Siberian Branch of the Russian Academy of Sciences, Akademgorodok 50/38, 660036 Krasnoyarsk, Russia

* **Correspondence**: Email: fom@icct.ru.

Abstract: Hollow glass-crystalline fly ash microspheres, commonly known as cenospheres, represent a promising material platform for developing composite membranes intended for gas mixture separation. In this work, the first comprehensive structural characterization of cenosphere-based microspherical membranes (CBMMs) was performed using scanning electron microscopy–energy-dispersive X-ray spectrometry (SEM-EDS), magic-angle spinning nuclear magnetic resonance (MAS NMR), Raman spectroscopy, photoluminescence spectroscopy, and Fourier transform infrared spectroscopy (FTIR). The cenosphere shells exhibited a fragmentary structure, pronounced chemical heterogeneity, and silicon-rich zones devoid of modifier elements. The glassy phase of the cenospheres, which contained approximately 10 mol% modifier ions, demonstrated a density of 2.2 g/cm^3, equivalent to that of pure silica glass, which contains no modifiers. This observed equivalence indicates an expanded glass network, resulting from the removal of modifier ions during the crystallization of defective phases within the glass-crystalline aluminosilicate shell. Furthermore, the close agreement between computational simulations and experimental FTIR spectra revealed the presence of strained structural sites and confirmed the formation of nanocavities attributable to the elimination of these modifier ions. To investigate the influence of the extended glass structure on the diffusion properties of silicate materials, the gas transport properties of the CBMMs were evaluated for pure gases (He, Ne) and for the He/Ne (80/20)

mixture. Single-gas permeation measurements revealed excellent performance, characterized by high helium permeability and a He/Ne ideal selectivity of 220–342 at 280 °C. Furthermore, single-stage membrane separation proved capable of enriching the helium feed from 80 to 99 vol%.

Keywords: cenosphere; silica glass; modified silica glass; expanded silica glass; helium–neon mixture; gas separation; permeability; selectivity

1. Introduction

The separation of noble gases, particularly helium and neon, constitutes a critically important task in the cryogenic industry, nuclear power engineering, and the production of high-purity specialty gases, among other fields [1]. The primary method for obtaining high-purity helium and neon is the energy-intensive cryogenic process [2]. In Russia, helium is extracted from natural and associated petroleum gases, which contain extremely low concentrations of helium, typically in the range of 0.04%–0.12%. This process involves the low-temperature condensation of the entire volume of natural gas to produce a helium concentrate, followed by several purification stages to remove impurities such as hydrogen, methane, nitrogen, argon, and neon from the obtained concentrate [2–4]. Adsorptive purification for neon removal is carried out at a low temperature of −196 °C and a high pressure of 15–20 MPa. The primary source of neon suitable for industrial production is atmospheric air, in which the volume fraction of neon is 18×10^{-4}%. Neon is obtained together with helium as a by-product during the liquefaction and fractionation of air; further separation of the neon–helium mixture is accomplished via low-temperature rectification.

Given that the production of high-purity helium and neon has traditionally been addressed using energy-intensive cryogenic methods, there is considerable interest in the development and refinement of alternative technologies. Moreover, membrane technology is gaining prominence in the field of gas separation and purification. Membrane gas separation does not entail significant energy consumption, which constitutes an indisputable advantage over conventional cryogenic technology. In addition to low energy requirements, key features include the simplicity of implementing membrane-based processes, their continuous operation, ease of integration with other process cycles, mild operating conditions, scalability, the absence of auxiliary additives, and straightforward process control [5].

The efficiency of membrane technology is largely determined by the permeability and selectivity of the membrane material, as well as its long-term stability under external influences. In the field of membrane materials science, at least two relevant and interrelated challenges have been identified: On the one hand, the improvement of the properties of membrane materials, and on the other hand, the development of novel membranes with enhanced microstructure and gas-transport characteristics [6].

Polymer membranes, which dominate the gas separation market, exhibit insufficient selectivity and thermal stability, thereby stimulating the search for alternative inorganic materials [7,8]. Moreover, hollow glass–crystalline microspheres derived from fly ash, namely cenospheres [9], have attracted considerable interest as promising materials for the fabrication of composite membranes [10,11]. However, the key challenge lies in the uncertainly of the permeability and selectivity mechanisms associated with the structure of the glass–crystalline shell of cenospheres, particularly concerning the

glass phase. Through the crystallization of defect phases, the composition of the glass phase in cenospheres can be modified by removing modifier ions that hinder diffusion, thereby transforming the structure of the membrane material and, consequently, enabling control over the selective gas transport process. It has been established that the permeability coefficients of the cenosphere glass phase for helium, hydrogen, and neon exceed the corresponding values for silicate glasses, while maintaining high selectivity. It has been hypothesized that the observed excess in the experimental permeability coefficients of the cenosphere glass phase over those of commercial silicate glasses is attributable to the formation of an expanded glass-phase structure. Nevertheless, an experimental investigation of the structure of the cenosphere glass phase has not been conducted.

To elucidate the influence of the expanded medium-range structure on the diffusion properties of silicate materials, a set of molecular models of silica glass with varying densities was constructed, and a theoretical evaluation of their diffusion properties was performed [12]. It was demonstrated that silica glass membranes with an expansion degree ranging from 10% to 14% exhibit high helium permeability combined with high He/Ne selectivity. It was theoretically established that the improvement in gas-transport properties compared with conventional silica glass is achieved through the formation of a specific microstructure of the membrane material, which enables the implementation of different diffusion mechanisms for the separated gases, namely super-diffusion for helium and normal or sub-diffusion for neon.

In this work, for the first time, the structure of glass–crystalline membrane materials based on fly ash cenospheres is investigated using a comprehensive set of modern physicochemical methods, with the aim of elucidating the structural peculiarities of the glass phase. In addition, the gas transport properties, including permeability coefficients, selectivity, and separation factor, were determined for these materials using both pure gases (He and Ne) and their binary mixture.

2. Materials and methods

2.1. Materials

Cenosphere-based microspherical membranes (CBMMs) were obtained using a previously developed technique involving the separation of cenosphere concentrates into narrow fractions [9] and high-temperature treatment of the resulting fractions [10,11].

The following samples were used for the study of glass microstructure:

- Silica glass: high purity fused silica, Corning® HPFS®, density ρ = 2.198 g/cm^3.
- Modified glass (MG): the initial narrow fraction of cenospheres with a size range of 50–63 μm, ρ = 2.349 g/cm^3.
- Expanded glass (EG): the narrow fraction of cenospheres with a size range of 50–63 μm after high-temperature treatment at 1100 °C, ρ = 2.212 g/cm^3.

The initial narrow cenosphere fraction was used as the starting modified sample MG. An expanded sample EG was obtained from this fraction by removing modifier ions from the glass phase via high-temperature treatment in an oxidizing atmosphere at 1100 °C for 3 h. The process can be represented as follows: modified sample MG → 1100 °C → expanded sample EG. Expanded glass is defined here as a glass phase whose density is lower than that of a glass of the same chemical composition prepared by conventional melting and quenching.

2.2. Methods

2.2.1. Membrane characterization

For CBMMs, we determined the following physicochemical characteristics: chemical and phase compositions, absolute density, and composition of the glass phase. The methods for determining these parameters are described in detail in [9–11].

The chemical composition, including the content of silicon, aluminum, iron, calcium, magnesium, potassium, and phosphorus oxides, was determined using chemical analysis according to the State Standard GOST 5382-2019 [13], which specifies the methods for component identification.

The phase composition was determined using quantitative X-ray powder diffraction analysis with the full-profile Rietveld method and derivative difference minimization, according to the procedure described in [9]. X-ray diffraction data were collected on an X'Pert Pro MPD powder diffractometer (PANalytical, Almelo, The Netherlands) equipped with a PIXcel solid-state detector using Cu-Kα radiation (2θ range 12–120°). The weight fraction of the X-ray amorphous component was determined by the external standard method, using corundum as the reference. Absorption coefficients were calculated from the total elemental composition obtained by chemical analysis.

The absolute density of CBMMs was measured by helium pycnometry. The relative error in density determination at a 95% confidence interval did not exceed 0.1%. The glass phase composition was calculated from chemical analysis and quantitative X-ray phase analysis data [11].

The structure of CBMMs was examined using TM-3000 and TM-4000 scanning electron microscopes (High Technologies Corporation, Hitachi, Japan). Elemental distribution was studied on polished cross-sections of cenospheres by SEM-EDS (scanning electron microscopy and energy-dispersive X-ray spectrometry). The analysis was performed on a TM-3000 SEM equipped with a Quantax 70 microanalysis system and a Bruker XFlash 430H energy-dispersive X-ray spectrometer, with measurements carried out in elemental mapping mode.

2.2.2. Nuclear magnetic resonance spectroscopy

Magic-angle spinning nuclear magnetic resonance (MAS NMR) spectra were recorded on a Bruker AVANCE III 600 spectrometer (Bruker, Germany) equipped with a broadband triple-channel MAS probe, using standard 3.2 mm ZrO_2 rotors. ^{29}Si and ^{1}H MAS spectra were acquired at operating frequencies of 119 and 600 MHz, respectively, with a sample spinning rate of 7.4 kHz. All spectra were processed in Topspin 3.2.

Spin–spin relaxation times (T_2) were measured on a NMReady-60e relaxometer (Nanalysis, Canada) with the standard Carr–Purcell–Meiboom–Gill (CPMG) pulse sequence using an interval of 30 μs between the 90° and 180° pulses. The decay of the echo amplitude (the relaxation curve) follows the familiar exponential law Eq 1 [14]:

$$I = I_0 exp(-\tau/T_2) \quad (1)$$

where I_0 is the signal intensity at zero echo time, I is the signal intensity, τ is the echo time, and T_2 is the spin–spin relaxation time.

Before the T_2 measurements, the samples were equilibrated in D_2O until saturation. Under these conditions all exchangeable hydrogens were replaced by deuterium (Si–OD) and became invisible in

the ^{1}H spectrum; the residual signal arose either from the HDO produced by the exchange or from protons that were inaccessible to it.

2.2.3. Raman and photoluminescence spectroscopy

Raman spectra were recorded between 200 and 2400 cm^{-1} in backscattering geometry on a scanning-probe nanolaboratory equipped with an NTEGRA SPECTRA IV spectrometer (NT-MDT BV). The scattered light was collected with a thermoelectrically cooled CCD detector. Excitation was provided by a diode-pumped solid-state laser (532 nm, 0.4 mW). The beam was focused through a Mitutoyo Plan Apo 100× objective (N.A. = 0.7) into a spot 1 μm in diameter, and the accumulation time per spectrum was 30 s. Photoluminescence spectra were measured on the same instrument under identical conditions over the range 550–850 nm.

2.2.4. Fourier transform infrared (FTIR) spectroscopy and two-dimensional correlation infrared spectroscopy (2T2D-COS)

FTIR spectra were recorded on a Vertex 70 spectrometer from KBr pellets at room temperature over the range 400–4000 cm^{-1} with a spectral resolution of 4 cm^{-1}. Post-processing comprised baseline correction and intensity normalisation. Far-infrared FTIR spectra were recorded over the range 100–700 cm^{-1} using a DLaTGS detector with a polyethylene (PE) window, multilayer beamsplitter, and dry nitrogen purging.

Two-dimensional correlation maps were computed from the processed spectra of the modified (S_1) and expanded (S_2) samples according to [15,16]. From the two prepared spectra, the difference spectrum $D(\nu) = S_1 - S_2$ was first evaluated. The synchronous map $\Phi(\nu_1, \nu_2)$ was obtained as the outer product of the difference spectrum with itself, $\Phi(\nu_1, \nu_2) = D(\nu_1) \times D(\nu_2)$. For the asynchronous map $\Psi(\nu_1, \nu_2)$, the Hilbert transform of the difference spectrum, $D'(\nu) = H[D(\nu)]$, was computed first, and the matrix $\Psi(\nu_1, \nu_2) = D'(\nu_1) \times D(\nu_2)$ evaluated from it. All calculations were performed in OriginLab 2024.

2.2.5. Calculation details

All calculations were carried out with the ORCA 6.0.1 program package [17]. The long-range-corrected hybrid functional with an empirical dispersion correction, ωB97X-D3 [18–20], was used in combination with the def2-TZVP basis set [21]. The RIJCOSX approximation was applied to accelerate the evaluation of the Coulomb and exchange integrals [22]. For every optimized structure, the Hessian matrix was computed, yielding harmonic vibrational frequencies together with IR absorption intensities.

Cyclic Si_nO_n fragments with n = 6–9 were taken as models, these being the most common ring sizes in the structure of ordinary silica glass [23]. The Si atoms were terminated with hydrogen atoms to ensure their valence was equal to 4. Four systems were calculated for each ring size: the bare ring (charge 0, multiplicity 1), the ring containing an Al^{3+} cation (charge +3, multiplicity 1), and the ring containing an Fe^{3+} cation in two spin states, high-spin (S = 5/2, multiplicity 6) and low-spin (S = 1/2, multiplicity 2).

2.2.6. Gas transport characterization

Single gas (He, Ne) permeation experiments were carried out in a static vacuum system, under conditions permitting gas diffusion into the internal cavities of the cenospheres. Gas transport through cenosphere shells was provided by the difference in partial pressures of the He or Ne outside and inside the globules. The measurements were carried out in the temperature range of 25–360 °C for helium and 280–500 °C for neon. The technique, including the determination of the He and Ne permeability coefficients, ideal selectivity, and diffusion activation energy, is described in detail in [10,11]. The relative standard error of permeability determination did not exceed 10%. The activation energy (E_a) was calculated from the experimental temperature dependence of the helium permeability coefficient, described by the Arrhenius equation.

The ideal selectivity of CBMMs was calculated as the ratio of the single gas permeability coefficients using Eq 2:

$$\alpha_{He/Ne} = K_{He}/K_{Ne} \quad (2)$$

where $\alpha_{He/Ne}$ is the selectivity; K_{He}, K_{Ne} is the permeability coefficients of He and Ne.

Membrane gas separation was studied using a binary He–Ne gas mixture containing 80 vol% He and 20 vol% Ne; this He content was close to that of the helium concentrate obtained by traditional cryogenic technology following low-temperature condensation of hydrocarbons [24]. The separation performance of CBMMs for the gas mixture was investigated using an ASAP 2020C-MP sorption analyzer (Micromeritics, USA). The concentrations of the gas mixture components (He and Ne) during desorption from the internal cavities of the cenospheres were recorded using a Hiden QGA mass spectrometer (Hiden Analytical, UK); the measurements were carried out at 280 °C in N_2 flow.

The volume concentration of He and Ne in the mixture with the carrier gas after passing through the glass-crystalline shell of the cenospheres was calculated from the area under the gas desorption curve. The helium content in the binary mixture obtained at the outlet was calculated using Eq 3 [25]:

$$V_{He} = \frac{C_{He}}{\sum C_i} \times 100\% \quad (3)$$

where V_{He} is the volume content of helium in permeate, C_{He} is the concentration of helium in N_2, and C_i is the sum of the concentrations of the components in the permeate of a binary He–Ne mixture in N_2.

The gas mixture selectivity of CBMMs toward the binary He–Ne gas mixture was characterized by the separation factor, which was calculated by Eq 4 [26]:

$$\beta_{He/Ne} = \frac{C_{He}/C_{Ne}}{C_{0He}/C_{0Ne}} \quad (4)$$

where $\beta_{He/Ne}$ is the separation factor; C_{He} and C_{Ne} are the concentrations of helium and neon in permeate, respectively; and C_{0He} and C_{0Ne} are the concentrations of helium and neon in the initial He-Ne mixture, respectively.

3. Results and discussion

3.1. Membrane composition and structure

The chemical and phase compositions of CBMMs are provided in Table 1. According to the chemical analysis, the CBMMs are a multicomponent system with a total content of the main macrocomponents, SiO_2 and Al_2O_3, of 95 wt%. The phase composition includes crystal phases and a glass phase. Among the crystal phases, there are those that were present in the original cenospheres (MG), mullite (0), and quartz (0). The mullite (I), quartz (I), *β*-cristobalite, and anorthite were formed after the high-temperature treatment (EG).

Table 1. Chemical and phase composition of CBMMs.

Sample	Chemical composition (wt%)								
	SiO_2	Al_2O_3	Fe_2O_3	CaO	MgO	SO_3	Na_2O	K_2O	P_2O_5
Modified	58.12	36.63	0.80	1.54	1.22	0.21	0.63	0.56	0.08
	Phase composition (wt%)*								
	Glass phase	Mullite (0)	Mullite (I)	Quartz (0)	Quartz (I)	Calcite	*β*-Crystobalite	Anortite	
Modified	68.2	30.1	–	1.4	–	0.3	–	–	
Expanded	30.2	37.2	13.0	0.3	2.2	–	14.7	2.4	

*Note: (0) is designation of crystal phases present in the initial sample, (I) is designation of the same phases formed after heat treatment at 1100 °C.

X-ray diffraction analysis of the newly formed crystalline phases revealed defects in their crystal structures [10,11]. During the additional heat treatment of cenospheres, the formation of mullite phase (I) in an oxidizing atmosphere was accompanied by the oxidation of Fe^{2+} to Fe^{3+}, which facilitated their extraction from the glass phase. These ions were then incorporated into the lattice of crystallizing mullite, replacing Al^{3+} ions. As a result, a defective iron-containing mullite phase (I) formed in the glass-crystalline shell of the cenospheres, which contributed to the further removal of modifier ions from the glass phase. The reason for the stabilization of the high-temperature form of *β*-cristobalite is a defect in its structure associated with the introduction of aluminum ions. The quartz phase, which also incorporates aluminum ions, is also defective; it forms upon dissolution of the initial quartz in the molten glass phase. The formation of anorthite, Ca-aluminosilicate, led to the depletion of calcium ions in the glass phase.

Based on the data of the chemical analysis and quantitative X-ray phase analysis (Table 1), the composition of the glass phase in CBMMs was calculated. The total content of oxide modifiers ($Na_2O + K_2O + CaO + MgO + Al_2O_3 + Fe_2O_3$) in the silicate glass matrix is 20.9 mol% for MG and half as much for EG, 9.6 mol% (Table 2). The density of the glass phase of the cenospheres, which contain ~10 mol% of modifier ions, is equivalent to that of silica glass ($\rho \sim 2.2$ g/cm^3), in which no modifier ions are present. This equivalence indicates that the glass phase has an expanded structure, which arises from the removal of modifier ions accompanying the crystallization of defective phases within the glass-crystalline aluminosilicate shell.

Table 2. Density and chemical composition of the glass phase in CBMMs.

Sample	Density(g/cm^3) ± 0.001, P = 0.95	Chemical composition (mol%)							
		SiO_2	Al_2O_3	Fe_2O_3	CaO	MgO	Na_2O	K_2O	P_2O_5
Modified	2.349	79.08	13.51	0.48	2.37	2.95	0.98	0.58	0.05
Expanded	2.212	90.27	0	0	1.68	5.54	1.25	1.10	0.16

SEM images of CBMMs are shown in Figure 1.

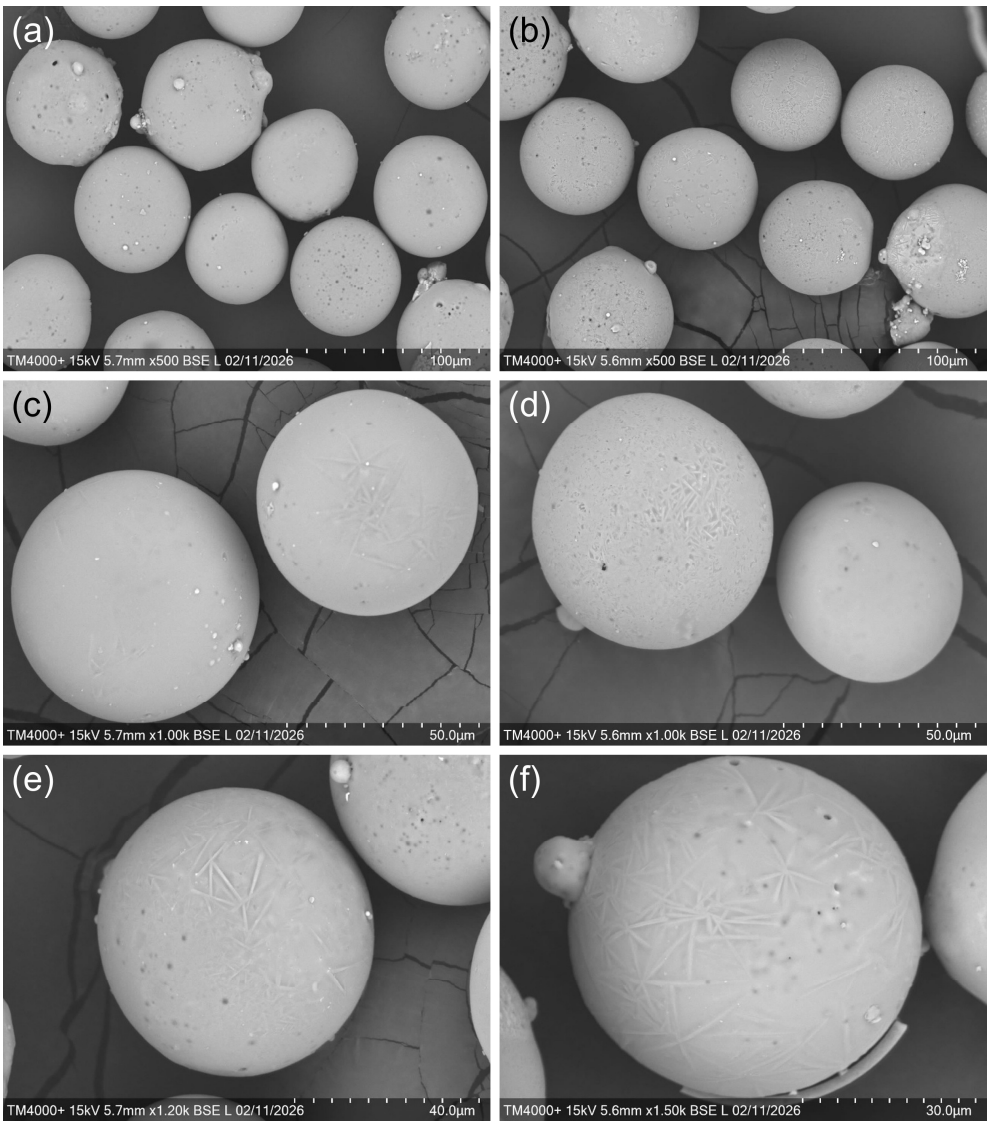


Figure 1. SEM images of CBMMs: (a, c, e) MG; (b, d, f) EG.

The cenosphere shell has a complex structure, comprising a glass-crystalline matrix and a 30–50 nm thick nanoscale film on both the outer and inner surfaces of the globules [10,11]. Needle-like mullite crystallites are observed beneath this film (Figure 1). SEM-EDS analysis reveals that the shell is fragmentary and chemically heterogeneous, with silicon-rich zones lacking modifier elements (Figure 2).

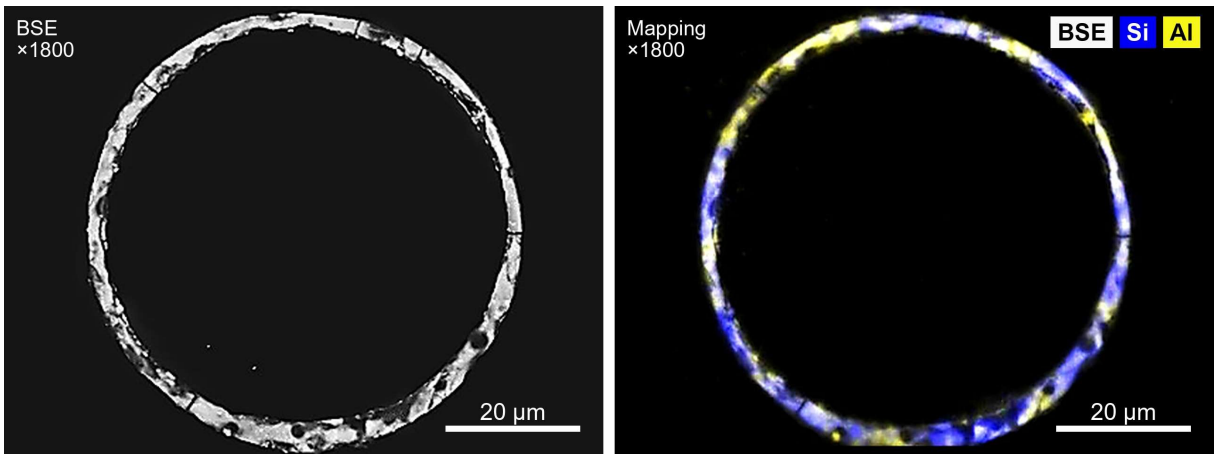


Figure 2. SEM images of polished section and Si/Al distribution maps in the cenosphere shell.

3.2. Glass structure investigation

3.2.1. NMR spectroscopy

The ^{1}H spectrum (Figure 3a) of the reference SiO_2 contains two well-resolved peaks, at 3 and 8 ppm, which belong to Si–OH silanol groups and to adsorbed water, respectively. In the modified sample, the hydroxyl signal shifts downfield to 3.8 ppm, indicating a change in the chemical environment of the silanol groups; furthermore, a set of lines appears at 7–9 ppm and is retained in the expanded sample. The 7–9 ppm group of signals is most probably attributed to strongly bound water and to the formation of aqua complexes with the modifier cations. The persistence of these lines in the spectrum of the expanded glass, i.e., after removal of the modifiers, provides evidence for the formation of cavities that retain water: The water remains within the structure, whereas the cations to which it was originally bound leave the sample.

The ^{29}Si spectrum (Figure 3b) of the pristine silica glass consists of a single broad line at −110 ppm, the typical signal of Q^4 silicon atoms in the disordered amorphous SiO_2 network. In the spectrum of the modified sample, a second component appears as a shoulder centered near −95 ppm, which is characteristic of Q^3 and/or Q^2 structural units and therefore provides direct evidence for rupture of the Si–O–Si network and formation of silanol groups [27]. The spectrum of the expanded sample differs substantially from both of the preceding spectra. The narrow line at −110.3 ppm corresponds to Q^4 in the ideal tetrahedral lattice of cristobalite [28]; the broad line underlying it, centred near −110 ppm, is attributed to disordered Q^4 atoms in the $Si(OSi)_4$ network of the amorphous glass phase [29]; and the broad line at −91 ppm, which represents the sum of the Q^2 and Q^3 contributions, indicates a high concentration of network-rupture defects (silanol groups) and correlates with the presence of a well-developed system of nanocavities formed after removal of the modifier ions.

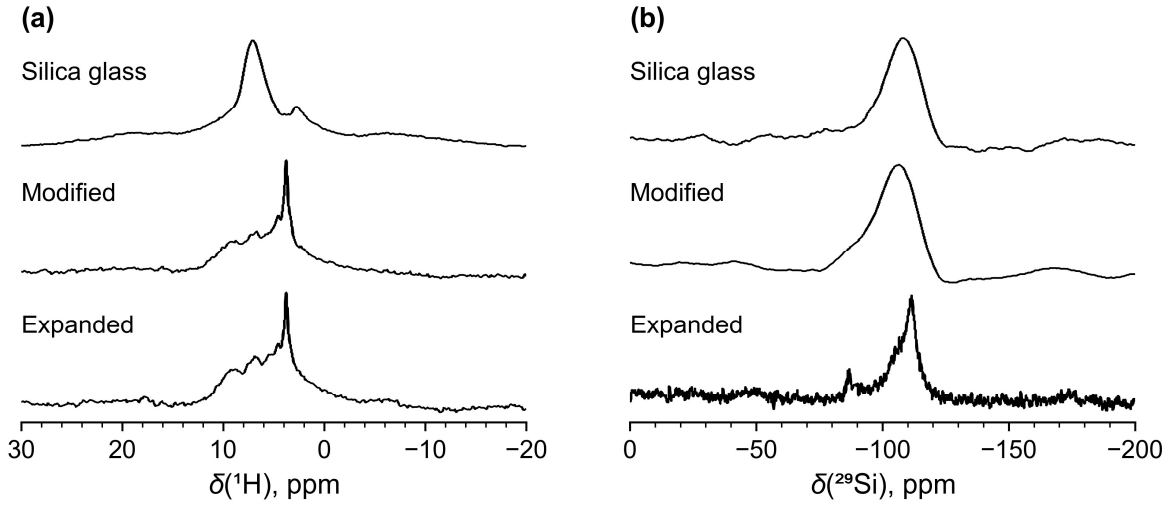


Figure 3. (a) ^{1}H and (b) ^{29}Si MAS NMR spectra of the samples studied (ω = 7.4 kHz).

The narrow line at −87 ppm calls for separate discussion. It lies in the range typical of T^3 (Si–C) structural units; however, ^{13}C CP-MAS and single-pulse experiments performed at a range of relaxation delays (D_1 = 5, 15, 50 and 180 s; 4000 scans accumulated) fail to detect any ^{13}C signal, even a weak one. An assignment to Si–C is therefore excluded. On the other hand, four silicon sites with signals at −86, −90, and −94 ppm and a shoulder near −80 ppm have been described in the literature for mullite solid solutions [30,31], which agrees well with the observed position of −87 ppm.

Quantitative analysis was performed following the procedure in [32]. Deconvolution used a set of Gaussian components; the component centers were allowed to shift within ±1.5 ppm of the nominal Q^n values, which prevented the intensity-stealing effect between the overlapping Q^3 and Q^4 contributions that occurs when the centers are held fixed (Figure S1). The quality of the fit was monitored through the coefficient of determination R^2 and the residual standard deviation (Table 3).

Table 3. Speciation of the Q^n structural units.

Sample	δ(Q^4) (ppm)	Fraction of Q^4 (%)	δ(Q^2/Q^3) (ppm)	Fraction of Q^2/Q^3 (%)	R^2
Silica glass	−107.3	100	—	0	0.9968
Modified	−109.5	96.9 ± 0.05	−93.5	3.1 ± 0.05	0.9963
Expanded	−112.5	88.3 ± 0.06	−90.9	11.7 ± 0.06	0.9926

The fraction of Q^2/Q^3 structural units, which correspond to broken network bonds and to silanol groups, increases steadily along the series pristine silica glass → modified sample → expanded sample: 0 → 3.1 → 11.7%. It is of fundamental importance that the maximum value is reached in the expanded sample, that is, after removal of the modifiers, and not in the modified one. This means that removal of the cations does not restore the original connectivity of the network; on the contrary, it leaves behind the highest concentration of rupture defects; exactly what is to be expected when the walls of nanocavities are exposed.

3.2.2. ^{1}H spin-spin relaxation

The relaxation curves of the expanded and modified samples (Figure 4) contain two components (regions of fast and slow decay are clearly distinguishable), whereas the curve of the silica glass is dominated by a single component, that of free, bulk-like water.

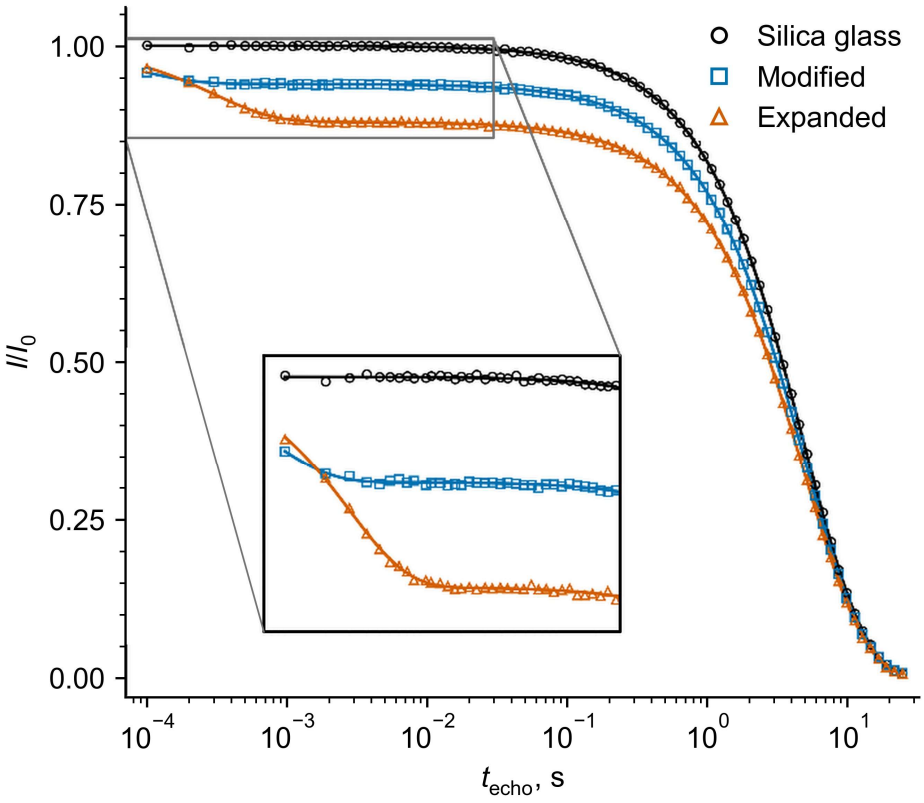


Figure 4. CPMG relaxation curves of the samples studied.

The slow component belongs to free water, whose state does not change from sample to sample; T_2 = 5 s is the standard value for it. The fast (rapidly decaying) component is assigned to bound, i.e., confined, water. In pure silica glass, which water does not penetrate, the second component does not appear (Table 4). This rules out any explanation of the fast components of the other two samples in terms of a processing artefact or of dephasing in internal field gradients, which would be identical for all samples.

Table 4. Components of the ^{1}H spin–spin relaxation.

Sample	Slow component T_2 (s)	Slow component fraction (%)	Fast component T_2 (μs)	Fast component fraction (%)
Silica glass	5.001 ± 0.004	99.95 ± 0.02	–	–
Modified	5.003 ± 0.004	94.48 ± 0.01	80 ± 11/3	5.52 ± 1.03
Expanded	4.996 ± 0.005	88.08 ± 0.02	275 ± 6.1	11.92 ± 0.2

Upon passing from the modified to the expanded sample, the fraction of the second component (more strongly bound water) and the relaxation time increase. The increase of T_2 is related to the removal of paramagnetic centres (annealing of iron). High-spin Fe (III) possesses five unpaired electrons and is a powerful sink for nuclear magnetization. Working with synthetic silicates of controlled Fe and Mn content, Foley et al. [33] showed that the relaxation rate of water protons is linearly proportional to the concentration of paramagnetic ions; they also established that a substantial surface relaxivity persists even in the absence of paramagnetic impurities, since the oxide surface relaxes nuclear spins efficiently.

3.2.3. Raman spectroscopy

The Raman spectrum of the pristine silica glass (Figure 5) corresponds to the classical spectrum of amorphous SiO_2: the antisymmetric stretching vibration of the bridging Si–O–Si bonds at 1100 cm^{-1}, the Si–OH stretching vibration at 970 cm^{-1} [34], the defect mode D_1 (~568 cm^{-1}, bending vibrations of four-membered $(Si–O)_4$ rings), the symmetric Si–O–Si deformation vibration at 460 cm^{-1} [35,36], and a low-frequency mode at 228 cm^{-1}.

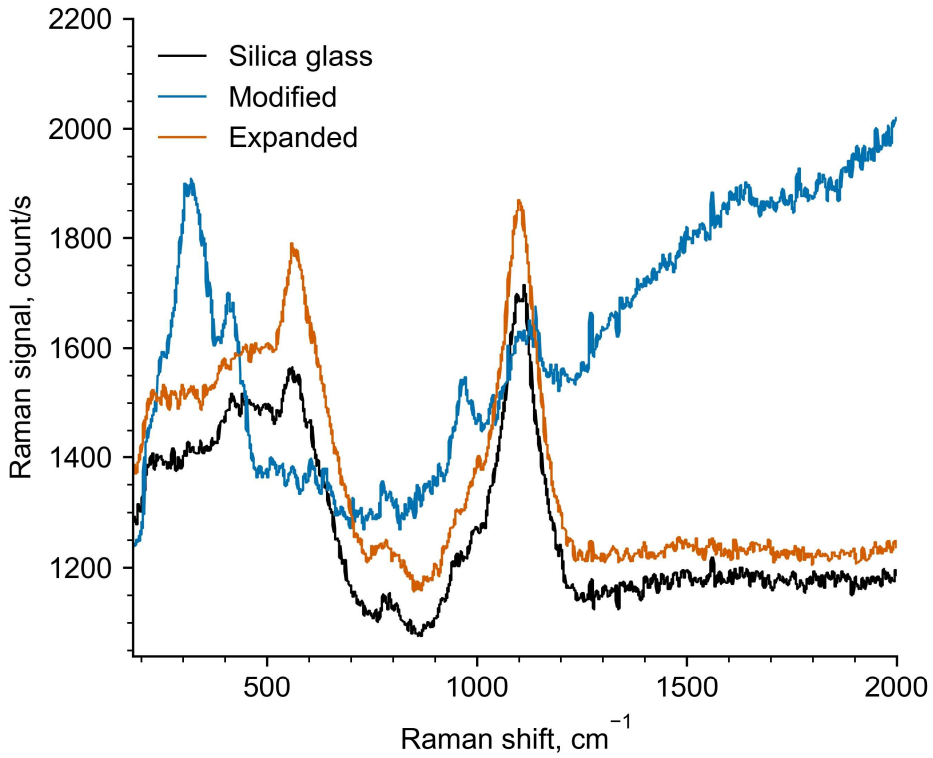


Figure 5. Raman spectra of the samples studied.

In the modified sample, bands appear at 310 cm^{-1} (O–Fe–O vibrations) [37,38] and at 607 and 797 cm^{-1} (ordered aluminosilicate fragments, including tetrahedrally coordinated Si–O–Al), together with shifted Si–OH (979 cm^{-1}) and Si–O–Si (1103 cm^{-1}) bands [39]. The bands at 1368 and 1600 cm^{-1} belong to vibrations of carbonate ions.

The spectrum of the expanded sample is practically identical to that of the pristine silica glass: The mullite and carbonate bands disappear. The absence of the characteristic β-cristobalite band near 420 cm^{-1} indicates a nanocrystalline or strongly defective state of this phase [40]. The set of weak,

broad overtone modes observed in the 1430–1890 cm^{-1} region is associated with the loss of translational symmetry at the boundaries of the nanocavities and at the amorphous-phase/nanocristobalite interfaces.

3.2.4. Photoluminescence (PL)

The PL spectrum of the pristine silica glass (Figure 6) is dominated by a broad band peaking at 633 nm with shoulders near 585 and 670 nm, characteristic of intrinsic oxygen-deficient centers in silica [41]. Both treated samples show a single broad maximum shifted to longer wavelength – 695 nm in the modified and 701 nm in the expanded sample, with a shoulder near 730 nm. The modified sample also retains weak intensity near 600 nm, which is absent in the expanded sample and may be associated with unstable radical centers formed during modification and subsequently annealed out.

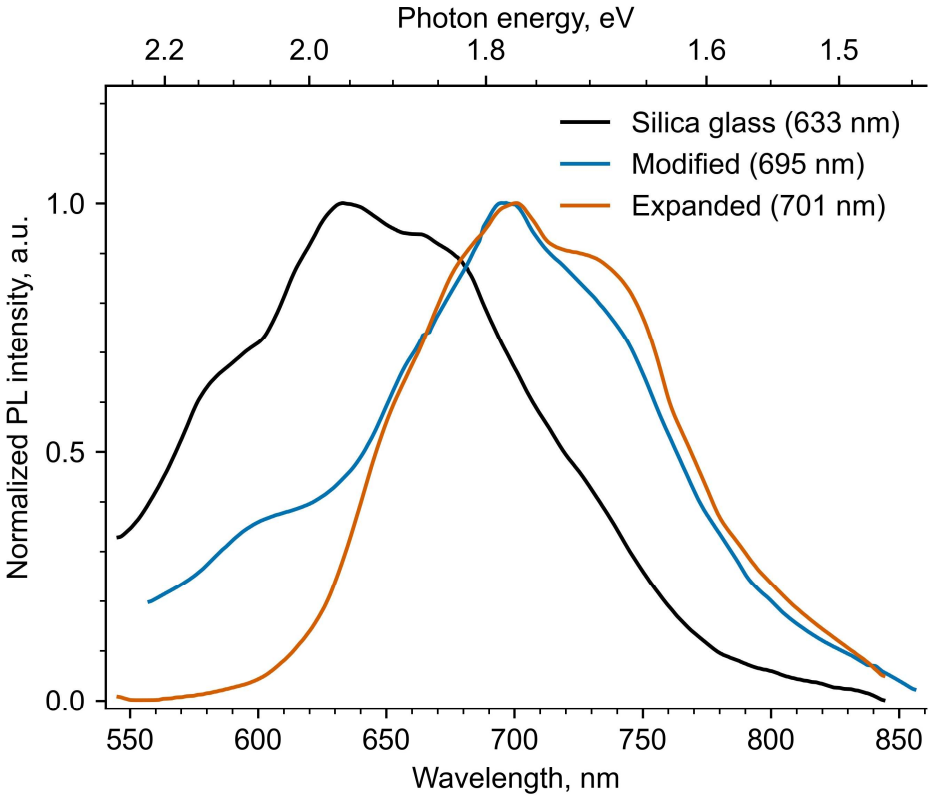


Figure 6. Photoluminescence spectra of the samples studied.

The signals at 685 and 720 nm are traditionally regarded as the "fingerprint" of the $^4T_1$–$^6A_1$ transition of iron (III) ions in tetrahedral or octahedral strong-field coordination [42]. However, the persistence of these lines in the expanded sample, from which the iron has been removed, contradicts such an assignment. Most probably these bands are associated with surface defects on the walls of the nanocavities (centres of the NBOHC, non-bridging oxygen hole centre, type) and/or with defects in nanocristobalite. The analogy with mesoporous and porous silica points to the sensitivity of such centers to the size and geometry of the cavities [43]. The weak band at 625 nm, which exists only in the modified sample, may be related to the formation of unstable radical centers during modification that are subsequently annealed out.

3.2.5. Infrared spectroscopy

The FTIR spectrum of the pristine silica glass (Figure 7a) contains the characteristic bands at 472 cm^{-1} (the transverse optical mode TO_1, rocking motions perpendicular to the Si–O–Si plane), 801 cm^{-1} (TO_2, symmetric stretching vibration) and 1082 cm^{-1} (TO_3, antisymmetric stretching vibration). The TO_3 mode exhibits longitudinal splitting caused by the long-range Coulomb interaction and appears with a shoulder at higher wavenumbers, at approximately 1207 cm^{-1}. An analogous shoulder accompanies the TO_1 mode and shows up as the signal at 562 cm^{-1}, which belongs to cyclic Si–O–Si structures. The signal at 1627 cm^{-1} is due to the bending vibrations of water. The vibrational modes of the Si–OH groups are represented by the shoulder of the stretching band at 960 cm^{-1} and by the broad band at 3300–3500 cm^{-1}, which contains contributions from isolated surface silanol groups (3500–3700 cm^{-1}) and from hydrogen-bonded Si–OH in chains (3200–3650 cm^{-1}) [44].

In the modified sample (Figure 7b), the long-wavelength region displays two strong, well-resolved bands at 465 and 557 cm^{-1} (the shift to longer wavelengths indicates a weakening of the Si–O–Si bonds upon incorporation of the modifiers), a set of overlapping bands in the 700–950 cm^{-1} range, weak modes at 1350–1500 cm^{-1} region (carbonate ions, in agreement with the Raman data [34]), and a the water bending mode shifts and splits into components at 1593 and 1696 cm^{-1} (strongly bound water and aqua complexes with the modifiers). In the silanol vibration region, the band narrows appreciably and develops a distinct maximum at 3451 cm^{-1}, accompanied by peaks at 3390 and 3260 cm^{-1}. In the expanded sample, after removal of the modifier ions, the TO_1 band shifts to 474 cm^{-1} and the band of the cyclic Si–O–Si units to 562 cm^{-1}; the 562 cm^{-1} line is resolved considerably better in the expanded sample than in the pristine glass. The 700–950 cm^{-1} region is preserved, but a defined signal near 800 cm^{-1} is absent. The water bending band returns to 1627 cm^{-1}. The strong bands between 950 and 1500 cm^{-1} do not change in intensity but broaden noticeably, and the carbonate modes observed at 1350–1500 cm^{-1} disappear. In the short-wavelength region, overlapping bands with maxima at 3235, 3430, and 3583 cm^{-1} are observed.

The two-dimensional correlation spectra were analyzed for the modified and expanded glasses; the pristine silica glass was not included. The synchronous map (Figure 7c) shows strong negative cross-peaks between the water bending band at 1600 cm^{-1} and the 900–500 cm^{-1} range, which contains the vibrations of the structural defects, δ(Si–OH) and cyclic Si–O–Si. The negative correlation means that removal of the modifier ions increases the intensity of the defect bands (the cavities open up and the number of silanol groups grows), while the intensity of $\delta(H_2O)$ falls at the same time. This is explained by the loss of part of the water in the form of aqua complexes together with the metal ions during annealing.

The strong positive cross-peak in the 500–900 cm^{-1} region is due to the simultaneous growth in intensity of the TO_1 and δ(Si–OH) bands on passing to the expanded sample. In the modified sample, the network is severely disrupted by the incorporated ions: the TO_1 mode is shifted downward, and its intensity is reduced. Once the ions have been removed, the network partially recovers, TO_1 gains intensity, and its frequency rises. Furthermore, the walls of the nanocavities are exposed, and these carry a large number of silanol groups, which give rise to a band near 900–950 cm^{-1}. The two processes therefore run in parallel: repair of the network and formation of a hydroxylated cavity surface.

Of particular interest is the very strong cross-peak at 583/511 cm^{-1}, which does not coincide with any band position in the parent one-dimensional spectra. This is typical of two-dimensional spectra, in which shoulders and hidden bands that are not resolved in the original spectrum because of broadening

become apparent. The band at 511 cm^{-1} corresponds to Si–O–Si in highly strained three-membered rings, and the band at 583 cm^{-1} to the D_2 mode of four-membered rings [45]. The positive correlation between them means that their intensities change synchronously on going from the modified to the expanded sample, that is, both types of strained fragment arise simultaneously. This is a sign of concerted relaxation of the strained rings during the formation of the nanoporous structure.

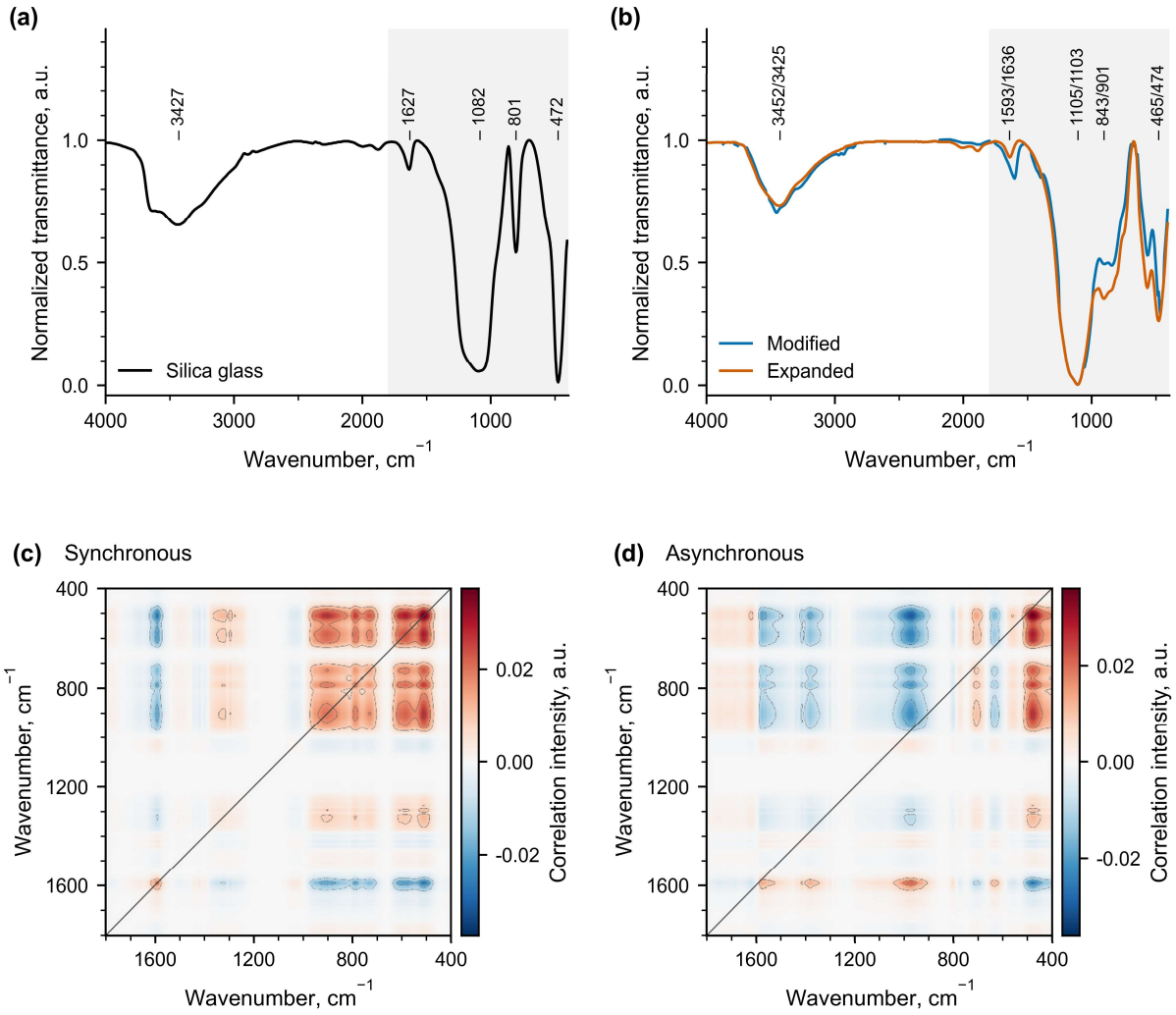


Figure 7. FTIR spectra: (a) silica glass (KBr pellet); (b) modified and expanded samples (KBr pellets); (c) synchronous 2T2D-COS correlation map; and (d) asynchronous 2T2D-COS correlation map.

The asynchronous correlation map (Figure 7d) reflects the sequence in which the intensities of the vibrational modes change on going from the modified to the expanded sample. Negative cross-peaks are observed at 970/530, 970/585, 970/737, 970/776, and 970/900 cm^{-1}. The negative sign means that ν(Si–OH) changes earlier than the defect modes at 500–900 cm^{-1}: The silanol groups are affected first, and only then do the cyclic structures and network defects rearrange. Furthermore, a set of positive correlations is seen at 470/500, 470/585, 470/720, 470/801, and 470/911 cm^{-1}, showing that ν(TO_1) changes earlier than the modes of the 500–900 cm^{-1} range. Consequently, the bending rigidity of the network is restored first, and only afterward do the characteristics of the Si–O stretching bonds (801

and 911 cm^{-1}) and of the cyclic structures (585 cm^{-1}) change. The water bending mode gives two cross-peaks, a weak negative one at 1600/470 and a weak positive one at 1600/978, which confirms the following sequence: weakly bound molecular water evaporates first, and dehydration of the surface through the removal of the aqua complexes of the modifier metals then leads to the formation of free Si–OH groups.

Analysis of the far-infrared region (Figure 8) reveals two circumstances essential for testing the hypothesis.

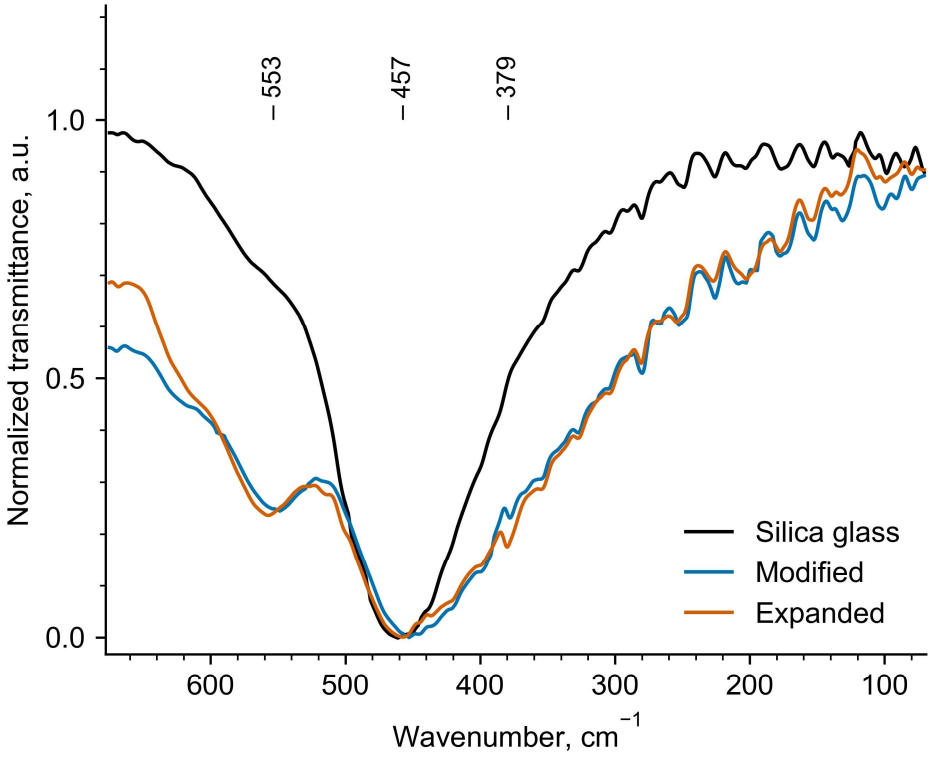


Figure 8. FTIR spectra in the far-infrared region.

First, the recovery of the short- and medium-range order is incomplete: the TO_1 minimum returns to within a few wavenumbers of the pristine value, a difference comparable to the spectral resolution and therefore not diagnostic in itself; yet, structural evidence points to incomplete recovery, since a band at 553 cm^{-1} (assigned to cyclic Si–O–Si units) is resolved in the modified and the expanded samples but appears only as an unresolved shoulder in the pristine glass, and a distinct band at 901 cm^{-1} persists in the expanded sample (Section 3.2.6).

Second, there is excess absorption in the 100–400 cm^{-1} region: the modified and expanded samples absorb substantially more strongly than the pristine silica glass across the 100–400 cm^{-1} range, and their spectra practically coincide; given that the expanded sample contains virtually no iron or aluminum, this excess absorption cannot arise from vibrations of metal–oxygen bonds and must be structural in origin. In glasses, absorption in this region is associated with disorder and medium-range heterogeneity (the boson-peak region) [46], so the observed effect points to a persistent nanoscale structural heterogeneity.

3.2.6. *Ab initio* simulation

For each ring size, the high-spin state of Fe^{3+} is the ground state, with the low-spin state lying higher by 21–27 kcal/mol (22.7, 21.5, 27.0, and 24.1 kcal/mol for n = 6, 7, 8 and 9, respectively), which corresponds to the weak field of the oxygen environment (Table S1). For n = 8 and 9, the optimized geometries of the two spin states are closely similar, differing by less than 0.03 Å in d(Fe–O) and by about 10 % in ring puckering. Only the high-spin results are used in the discussion that follows.

Geometry optimization revealed a fundamentally different behavior of the rings upon introducing of Al^{3+} and Fe^{3+} (Figure 9). The bare $(SiO)_n$ rings with n = 6–9 retain the original cyclic topology: each silicon atom is bonded to exactly two oxygen atoms, the Si–O bond length is 1.65 Å, and no strained fragments are present. As n increases, the mean bridging angle relaxes from 177.8° to 158–160°, close to the range characteristic of vitreous silica, and the ring becomes progressively puckered (Table S2). Incorporation of a cation rearranges the ring topology, and the nature of the rearrangement differs between aluminum and iron.

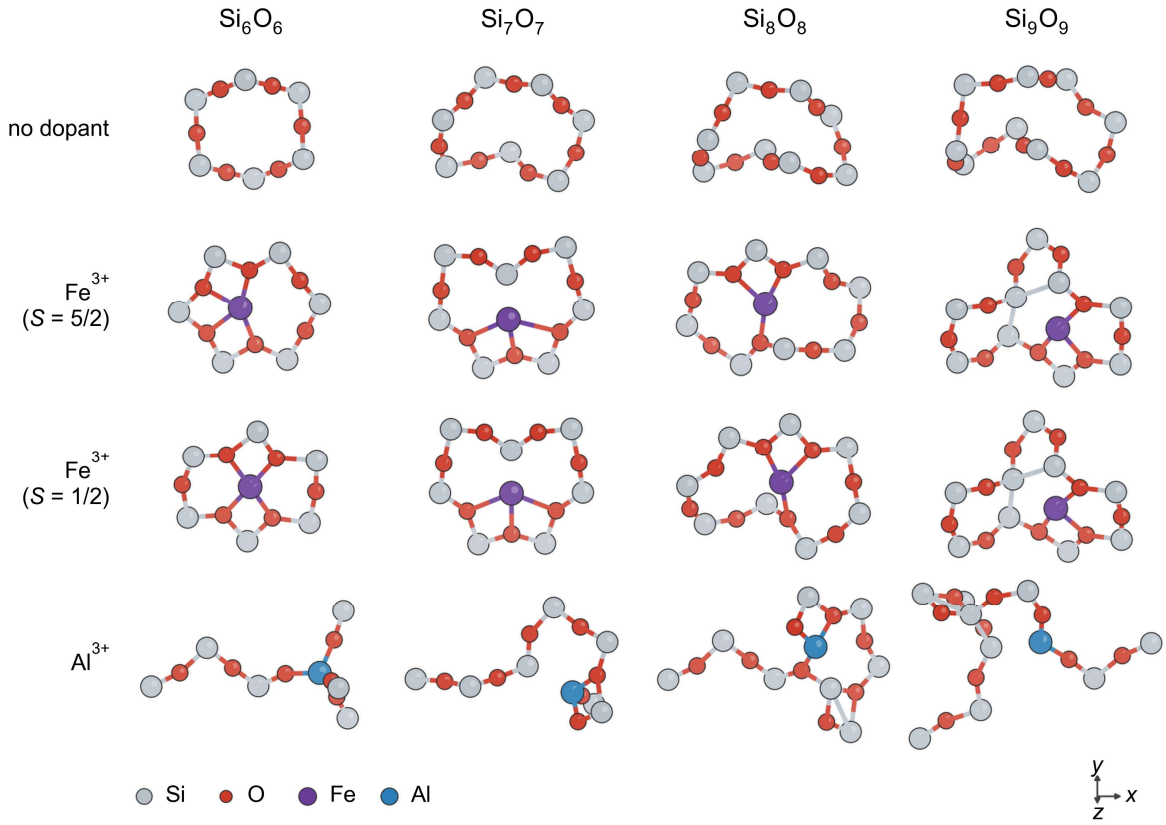


Figure 9. Optimized geometries of the bare $(SiO)_n$ clusters and of the clusters containing modifier cations (hydrogen atoms are hidden).

The iron (III) ion planarizes the ring, taking up a position at its center and becoming four-coordinate. For the large rings (n = 8 and 9), the ring is too large to close around the cation, so the iron ion remains three-coordinate, and the ring retains its puckered shape. The Fe^{3+} cation therefore organizes small rings into flat, chelate-like complexes, whereas with large rings, it forms only surface-type adducts.

Although aluminum can either be incorporated into the network or act as a coordinated modifier, the modeling shows that only incorporation into the network is a genuinely favorable process. In doing so, aluminum ruptures the rings and forms silanone-type Si=O double bonds (1.547–1.555 Å) rather than single Si–O bonds (1.65 Å). Four such bonds are present in the Si_6 structure, two in Si_7 and Si_9, and one in Si_8. With iron, by contrast, no such bonds are formed. In driving this structural rearrangement, aluminum creates small rings containing the Si–Al–O structural unit, as well as strained edge-sharing two-membered fragments built exclusively from silicon atoms. Thus, small rings are simply destroyed by aluminum, whereas it is precisely the large rings that are transformed into stable strained fragments consisting only of Si atoms.

The difference in the behavior of the two cations has a direct physical consequence: when the modifier is removed, the iron-containing coordination fragments disappear with the cation, and the network is free to relax, whereas the siliceous strained fragments created by aluminum contain no metal and are therefore preserved. The calculations thus identify aluminum as the structurally significant modifier, responsible for the residual "structural memory", which is consistent with the experimental observation that aluminum passes completely into the crystalline phase while the structural changes in the glass phase are retained.

The ring-size dependence noted above, purely siliceous strained fragments arise only in the large rings (n = 8, 9) and not in the small ones (n = 6, 7), agrees with the view that small (three- and four-membered) rings are not native structural elements of ordinary silica glass but are formed as a result of the incorporation of aluminum into the network.

To establish the link between the calculated structures and the experimental bands, the localization of the normal modes was analyzed: for each mode, the fraction of the kinetic energy residing on the atoms of the strained fragment was computed (all IR modes shown in Table S3–S5). The modes localized on the purely siliceous two-membered fragment by more than 80% are listed in Table 5, together with the mode at 589.7 cm^{-1} (70% localisation), which is relevant to the 2T2D-COS analysis discussed above.

Table 5. Vibrational modes localized on the purely siliceous two-membered fragment.

System	Wavenumber (ν, cm^{-1})	Integrated IR absorption intensity (I, km/mol)	Localisation (%)
$(SiO)_9 + Al^{3+}$	892.5	336	90
$(SiO)_9 + Al^{3+}$	873.5	61	94
$(SiO)_9 + Al^{3+}$	698.0	276	82
$(SiO)_9 + Al^{3+}$	589.7	32	70
$(SiO)_8 + Al^{3+}$	853.7	180	97

The reported IR markers of edge-sharing two-membered siloxane fragments on a dehydroxylated silica surface form a doublet at 888 and 907 cm^{-1} [47, 48]. The calculated modes at 873.5 and 892.5 cm^{-1}, which are 90–94% localized on such a fragment, reproduce this doublet without any adjustment to the experimental values. This assignment explains the persistence of the 700–950 cm^{-1} region in the IR spectrum of the expanded sample: these bands originate from strained, purely silicon–oxygen fragments rather than from Si–O–M bonds. This is why they survive the removal of the modifiers, a fact that cannot be accounted for by an assignment to Si–O–M. The mode at 589.7 cm^{-1}, which is 70% localized on the same fragment, corresponds to the 583 cm^{-1} cross-peak on the synchronous 2T2D-COS map.

The physical meaning of this assignment is fundamental to our hypothesis of this work. Two- and three-membered siloxane rings are the canonical product of the condensation of vicinal silanol groups on a dehydroxylated silica surface at temperatures above ~650 °C [49,50]. Their appearance is evidence not of densification of the structure but rather of the creation of new internal surface. In other words, the strained fragments observed here are the walls of the cavities. In addition, the integrated IR absorption intensity in the 100–400 cm^{-1} range averages 147 km/mol for the bare rings and rises to 361 km/mol upon introduction of Al^{3+} (a factor of 2.45) and to 208 km/mol upon introduction of Fe^{3+} (a factor of 1.41).

Modes in which the cation participates by more than 15% account for only 0–84 km/mol of the total increase. It follows that the enhancement of the far-infrared absorption is caused not by vibrations of metal–oxygen bonds but by the activation of framework modes as a result of symmetry breaking and the formation of strained fragments. This is why the excess absorption survives the removal of the cations, which corresponds exactly to the experimental observation that the curves of the modified and expanded samples coincide in the 100–400 cm^{-1} region. In addition, the bare rings show a monotonic dependence of the position of the dominant Si–O stretching vibration on ring size: 1032, 1001, 958, and 956 cm^{-1} for n = 6, 7, 8, and 9, respectively. The red shift with increasing ring size corresponds to the release of strain and is physically consistent.

Moreover, in the modified sample, the 700–950 cm^{-1} region is dominated by a band at 843 cm^{-1}, which shifts to 901 cm^{-1} in the expanded sample. This +58 cm^{-1} displacement is reproduced by the calculations: the edge-sharing two-membered fragment containing the cation (Si–Al) exhibits a band at 827 cm^{-1}, whereas the purely siliceous edge-sharing fragment exhibits a band at 892.5 cm^{-1}, giving a calculated shift of +65 cm^{-1} (Table S6). The experimental position of 901 cm^{-1} falls within the literature doublet at 888 and 907 cm^{-1} that identifies edge-sharing two-membered siloxane rings on a dehydroxylated silica surface [49,50]. The band therefore is not merely retained after removal of the modifiers: Its composition changes as predicted, with the cation-containing strained unit converting into a purely silicon–oxygen one.

3.3. Gas transport properties

Silicate glass-based materials with high selectivity are considered promising candidates for gas-separation membranes aimed at producing high-purity helium [2,6,8]. The gas transport behavior of silicate membrane materials depends on the composition and structure, which dictate gas migration through the modifier-ion-free interstitial spaces of the (SiO_4)-tetrahedra-based glass network [51,52]. Experimental data on helium diffusion through silicate glasses of varying compositions indicate that the helium permeability decreases considerably with increasing modifier oxide content [52]. Glass–crystalline membranes can possess improved gas permeability due to the purification of the glass phase from modifier ions [10–12].

The temperature dependences of the CBMMs permeability coefficients for He and Ne single gases in the 25–280 °C range are shown in Figure 10. High-temperature treatment of the cenosphere sample EG results in increased permeability coefficients for the studied gases throughout the temperature range relative to the untreated cenospheres MG.

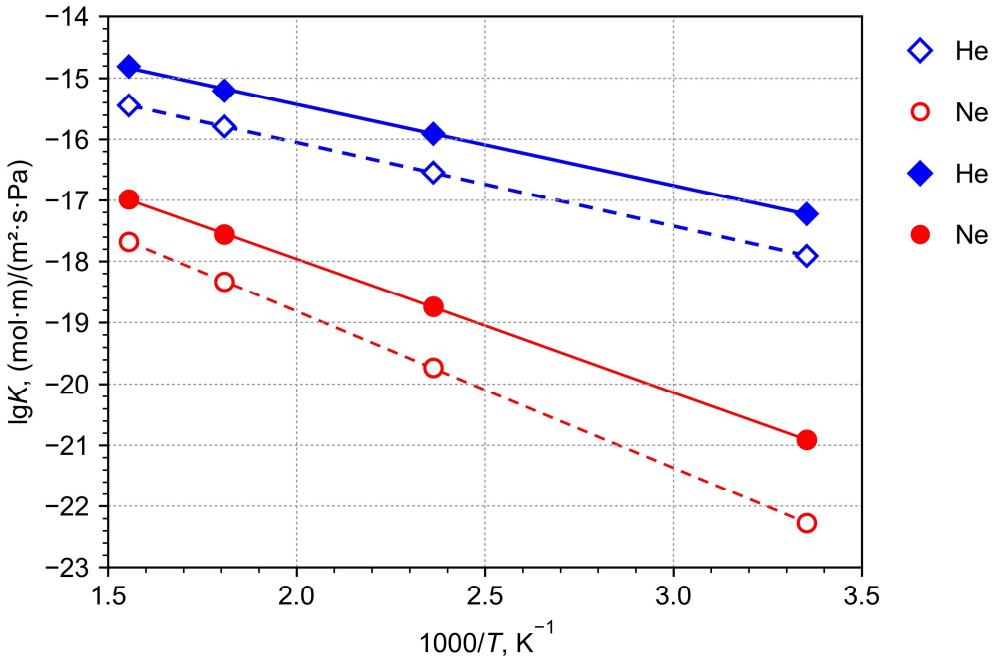


Figure 10. Temperature dependence of the He and Ne permeability coefficients for the CBMMs: MG – open symbols; EG – closed symbols.

A comparison of the gas permeability of the CBMMs with that of synthetic silicate glasses [52–55] at 280 °C (Table 6) shows that the helium permeability coefficient of EG is six times higher than that of Corning® #7056 glass, which contains the same amount of modifier oxide (10 mol%) but has a higher density of 2.29 g/cm^3 [52]. The activation energies determined for the CBMMs (Table 6), being comparable to the values for pure silica glass, suggest that gas diffusion occurs readily in the glass–crystalline membrane materials.

Gas mixture selectivity is a major factor in the practical application of membrane materials. The CBMM exhibits high He/Ne selectivity, with values of 220–342 at 280 °C (Table 6). These values are comparable to the selectivity of silica glass ($\alpha_{He/Ne}$ = 237–300) [54,55] and are substantially higher than those typical of other membrane materials, including polymers [56], metal–organic frameworks [57], and zeolites [58], where the values generally range from 1 to 2.

Table 6. Comparison of helium permeability and He/Ne ideal selectivity between the CBMMs and silicate glasses at 280 °C.

Sample	SiO_2 (mol%)	K_{He} (mol·m)/(m^2·s·Pa)	E_aHe (kJ/mol)	E_aNe (kJ/mol)	$\alpha_{He/Ne}$	References
Modified	79	1.6×10^{-16}	26	49	342	This work
Expanded	90	6.1×10^{-16}	25	42	220	This work
Corning glass	90	1.1×10^{-16}	–	–	–	[52]
Vycor glass	96	6.7×10^{-16}	–	–	276	[53]
Silica glass	100	1.3×10^{-15}	21	38	237–300	[54,55]

The gas separation performance of CBMMs toward a binary He–Ne mixture (80:20 vol%) was also studied (Figure 11, Table 7). Figure 11 shows the concentration changes of He and Ne in the N_2

stream during the experiments. The helium content in the outlet mixture after separation, calculated using Eq 3, is summarized in Table 7. Single-stage separation yields a separation factor of 12–25 (Eq 4), with the helium content in the permeate reaching 98–99 vol%. The activation energy data (Table 6) suggest that reducing the operating temperature of the membrane separation process should increase the separation factor and improve the purity of the desired component.

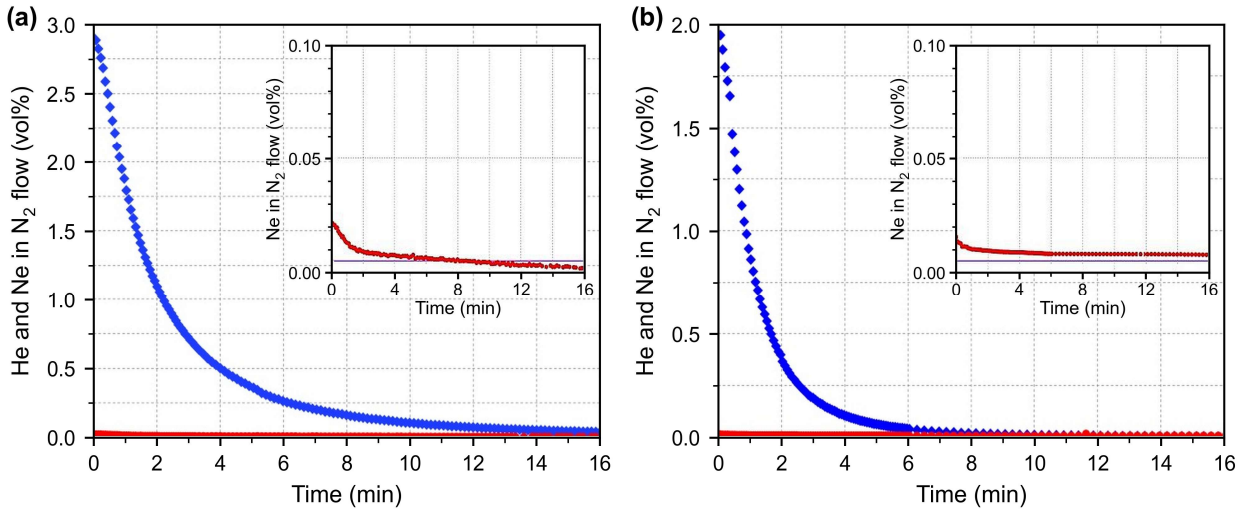


Figure 11. Desorption profiles of He (♦) and Ne (●) from CBMMs in N_2 flow at 280 °C: (a) MG; and (b) EG.

Table 7. Helium concentration in the permeate and separation factor of the He/Ne (80:20 vol%) binary mixture at 280 °C for the CBMMs.

Sample	C_{He} (vol%)	$\beta_{He/Ne}$
Modified	99	25
Expanded	98	12

It was shown [14] that in low-density (or expanded) fused silica, above a certain threshold of glass expansion, the diffusion behavior of dissolved helium atoms changes radically; from normal Brownian diffusion to super-diffusion. Neon, by contrast, migrates via normal or even sub-diffusion. This results in a substantial increase in the helium permeability coefficient and the He/Ne selectivity of such glasses. The glass phase of the CBMMs consists of more than 90% silica and is expanded compared with glasses of the same composition prepared by conventional methods (melting and melt quenching). Thus, the structure of the silicon–oxygen tetrahedral network in the CBMMs may be analogous to that of low-density fused silica. This suggests that the migration of helium and neon in these glasses may occur via the mechanisms described in [12].

The advantages of CBMMs include the fragmentary structure of the cenosphere shell, the presence of regions enriched in the glass-forming oxide SiO_2, and an expanded glass phase. The combination of high selectivity and permeability makes CBMMs a promising material for membrane gas separation and purification. Additional advantages include thermal stability, high mechanical strength of the glass–crystalline shell owing to mullite crystallites, and economic efficiency resulting from the use of thermal power plant waste as a feedstock. Membrane technology is inherently

modular, enabling capacity expansion by adding modules; a significant advantage over centralized cryogenic plants with high capital costs and long lead times. Membrane separation operates near ambient or moderately elevated temperatures, avoiding the substantial refrigeration duty required for cryogenic distillation.

4. Conclusions

Cenospheres have shown promise for composite gas-separation membranes. A comprehensive structural analysis of CBMMs has revealed a fragmentary, chemically heterogeneous shell with silicon-rich, modifier-depleted regions. Despite containing ~10 mol% modifier ions, the glass phase exhibits a density equal to that of silica glass, indicating an expanded structure.

In ^{29}Si NMR spectra, the fraction of Q^2/Q^3 structural units, which correspond to broken network bonds and to silanol groups, increases steadily from 0% in pristine silica glass to 3.1% in the modified sample and to 11.7% in the expanded sample. The monotonic red shift of the dominant stretching vibration in the FTIR spectra with increasing ring size (1032 → 1001 → 958 → 956 cm^{-1}) is accompanied by relaxation of the mean bridging angle (177.8 → 164.2 → 158.3 → 159.7°). The shift therefore reflects the release of angular strain rather than the ring size as such. Incorporation of a cation rearranges the ring topology, and the nature of the rearrangement differs between aluminum and iron.

The Fe^{3+} cation therefore organizes small rings into flat, chelate-like complexes, while with large rings, it forms only surface-type adducts. In driving this structural rearrangement, aluminum creates small rings containing the Si–Al–O structural unit as well as strained edge-sharing two-membered fragments built exclusively from silicon atoms. Small rings are thus simply destroyed by aluminum, whereas it is precisely the large rings that are transformed into stable strained fragments consisting only of Si atoms. The consistent results of calculations and experimental IR modes show the existence of strained structural sites and the formation of nanocavities during the removal of modifier ions.

Furthermore, single-gas permeation tests reveal high helium permeability and a He/Ne ideal selectivity of 220–342 at 280 °C. Gas separation experiments with the He/Ne mixture show that a single-stage membrane separation enriches the helium content from 80 to 99 vol%. Based on the activation energy data, lowering the operating temperature of the membrane separation process is expected to raise the separation factor and increase the purity of the target gas.

Use of AI tools declaration

The authors declare they have not used Artificial Intelligence (AI) tools in the creation of this article.

Acknowledgments

This work was conducted within the framework of the budget project FWES 2026–0011 for the Institute of Chemistry and Chemical Technology SB RAS. The characterization of glass microstructure was performed using equipment from the Krasnoyarsk Regional Research Equipment Center of SB RAS (FRC KSC SB RAS).

Author contributions

Elena V. Fomenko: conceptualization, visualization, writing–original draft, writing–review & editing, project administration, supervision; Timur Yu. Ivanenko: data curation, formal analysis, investigation, methodology, software, validation, visualization, writing–original draft, writing–review & editing; Sergey V. Kukhtetskiy: methodology, validation, writing–review & editing; Nikolay P. Shestakov: formal analysis, investigation; Alexander S. Krylov: formal analysis, investigation; Leonid A. Solovyov: formal analysis, investigation; Tatiana A. Vereshchagina: project administration.

Conflict of interest

The authors declare no conflicts of interest.

References

1. Kerry FG (2007) *Industrial Gas Handbook: Gas Separation and Purification*, 1st Eds., Boca Raton: CRC Press. https://doi.org/10.1201/9781420008265
2. Rufford TE, Chan KI, Huang SH, et al. (2014) A review of conventional and emerging process technologies for the recovery of helium from natural gas. *Adsorpt Sci Technol* 32: 49–72. https://doi.org/10.1260/0263-6174.32.1.49
3. Kim D, Gundersen T (2015) Helium extraction from LNG end-flash. *Chem Eng Trans* 45: 595–600. https://doi.org/10.3303/CET1545100
4. Jahromi PE, Fatemi S, Vatani A, et al. (2018) Purification of helium from a cryogenic natural gas nitrogen rejection unit by pressure swing adsorption. *Sep Purif Technol* 193: 91–102. https://doi.org/10.1016/j.seppur.2017.11.002
5. Jin D, Xiao G, Lu Z, et al. (2026) Industrial advances in helium recovery and purification technologies: A review. *Sep Purif Technol* 380: 135136. https://doi.org/10.1016/j.seppur.2025.135136
6. Scholes CA, Ghosh UK (2017) Review of membranes for helium separation and purification. *Membranes* 7: 9. https://doi.org/10.3390/membranes7010009
7. Soleimany A, Hosseini SS, Gallucci F (2017) Recent progress in developments of membrane materials and modification techniques for high performance helium separation and recovery: A review. *Chem Eng Process Process Intensif* 122: 296–318. https://doi.org/10.1016/j.cep.2017.06.001
8. Scholes CA (2018) Helium recovery through inorganic membranes incorporated with a nitrogen rejection unit. *Ind Eng Chem Res* 57: 3792–3799. https://doi.org/10.1021/acs.iecr.8b00314
9. Fomenko EV, Anshits NN, Solovyov LA, et al. (2013) Compositions and morphology of fly ash cenospheres produced from the combustion of Kuznetsk coal. *Energy Fuels* 27: 5440–5448. https://doi.org/10.1021/ef400754c
10. Fomenko EV, Rogovenko ES, Solovyov LA, et al. (2014) Gas permeation properties of hollow glass-crystalline microspheres. *RSC Adv* 4: 9997–10000. https://doi.org/10.1039/C3RA47909A

11. Fomenko EV, Rogovenko ES, Anshits NN, et al. (2023) Characterization of silicate glass/mullite composites based on coal fly ash cenospheres as effective gas separation membranes. *Materials* 16: 6913. https://doi.org/10.3390/ma16216913
12. Kukhtetskiy SV, Fomenko EV, Anshits AG (2023) Anomalous diffusion of helium and neon in low-density silica glass. *Membranes* 13: 754. https://doi.org/10.3390/membranes13090754
13. GOST 5382-2019 (2019) Cements and Materials for Cement Production. Chemical Analysis Methods. Moscow: Publishing House of Standards (in Russian). https://docs.cntd.ru/document/1200168999
14. Günther H (2013) *NMR Spectroscopy: Basic Principles, Concepts and Applications in Chemistry*, 3 Eds., Weinheim: Wiley-VCH.
15. Noda I (2018) Two-trace two-dimensional (2T2D) correlation spectroscopy—A method for extracting useful information from a pair of spectra. *J Mol Struct* 1160: 471–478. https://doi.org/10.1016/j.molstruc.2018.01.091
16. Noda I (2020) Closer examination of two-trace two-dimensional (2T2D) correlation spectroscopy. *J Mol Struct* 1213: 128194. https://doi.org/10.1016/j.molstruc.2020.128194
17. Neese F (2025) Software update: The ORCA program system—Version 6.0. *WIREs Comput Mol Sci* 15: e80019. https://doi.org/10.1002/wcms.70019
18. Lin YS, Li GD, Mao SP, et al. (2013) Long-range corrected hybrid density functionals with improved dispersion corrections. *J Chem Theory Comput* 9: 263–272. https://doi.org/10.1021/ct300715s
19. Chai JD, Head-Gordon M (2008) Long-range corrected hybrid density functionals with damped atom–atom dispersion corrections. *Phys Chem Chem Phys* 10: 6615–6620. https://doi.org/10.1039/b810189b
20. Grimme S, Antony J, Ehrlich S, et al. (2010) A consistent and accurate ab initio parametrization of density functional dispersion correction (DFT-D) for the 94 elements H–Pu. *J Chem Phys* 132: 154104. https://doi.org/10.1063/1.3382344
21. Weigend F, Ahlrichs R (2005) Balanced basis sets of split valence, triple zeta valence and quadruple zeta valence quality for H to Rn: Design and assessment of accuracy. *Phys Chem Chem Phys* 7: 3297–3305. https://doi.org/10.1039/b508541a
22. Neese F, Wennmohs F, Hansen A, et al. (2009) Efficient, approximate and parallel Hartree–Fock and hybrid DFT calculations. A 'chain-of-spheres' algorithm for the Hartree–Fock exchange. *Chem Phys* 356: 98–109. https://doi.org/10.1016/j.chemphys.2008.10.036
23. Xiang Y, Du J, Smedskjaer MM, et al. (2013) Structure and properties of sodium aluminosilicate glasses from molecular dynamics simulations. *J Chem Phys* 139: 044507. https://doi.org/10.1063/1.4816378
24. Yang J, Zavabeti A, Yu Z, et al. (2025) High purity helium and hydrogen production from natural hydrogen reservoir and natural gas. *Sep Purif Technol* 375: 133812. https://doi.org/10.1016/j.seppur.2025.133812
25. McNaught AD, Wilkinson A (1997) *IUPAC. Compendium of Chemical Terminology (the "Gold Book")*, 2 Eds., Oxford: Blackwell Scientific Publications. https://doi.org/10.1351/goldbook
26. Mulder M (1996) *Basic Principles of Membrane Technology*, 2 Eds., Dordrecht: Kluwer Academic Publishers. https://doi.org/10.1007/978-94-009-1766-8

27. Malfait WJ, Halter WE, Verel R (2008) ^{29}Si NMR spectroscopy of silica glass: T_1 relaxation and constraints on the Si–O–Si bond angle distribution. *Chem Geol* 256: 269–277. https://doi.org/10.1016/j.chemgeo.2008.06.048
28. Graetsch H, Mosset A, Gies H (1990) XRD and ^{29}Si MAS-NMR study on some non-crystalline silica minerals. *J Non-Cryst Solids* 119: 173–180. https://doi.org/10.1016/0022-3093(90)90840-I
29. Dupree R, Holland D, McMillan PW, et al. (1984) The structure of soda-silica glasses: A MAS NMR study. *J Non-Cryst Solids* 68: 399–410. https://doi.org/10.1016/0022-3093(84)90020-6
30. Jaymes I, Douy A, Massiot D, et al. (1996) Evolution of the Si environment in mullite solid solution by ^{29}Si MAS-NMR spectroscopy. *J Non-Cryst Solids* 204: 125–134. https://doi.org/10.1016/S0022-3093(96)00414-0
31. Gomes S, François M (2000) Characterization of mullite in silicoaluminous fly ash by XRD, TEM, and ^{29}Si MAS NMR. *Cem Concr Res* 30: 175–181. https://doi.org/10.1016/S0008-8846(99)00226-4
32. Sobornova VV, Khodov IA (2026) Quantitative ^{29}Si NMR spectroscopy of ordered mesoporous silicas: revisiting Q_3/Q_4 ratios and surface hydroxylation in SBA-15 and MCM-41. *Phys Chem Chem Phys* 28: 3540–3549. https://doi.org/10.1039/D5CP03966E
33. Foley I, Farooqui SA, Kleinberg RL (1996) Effect of paramagnetic ions on NMR relaxation of fluids at solid surfaces. *J Magn Reson Ser A* 123: 95–104. https://doi.org/10.1006/jmra.1996.0218
34. Chen X, Feng W, Zhang G, et al. (2019) Raman spectra of quartz and Pb^{4+}-doped SiO_2 crystals at different temperature and pressure. *Crystals* 9: 569. https://doi.org/10.3390/cryst9110569
35. Boizot B, Agnello S, Reynard B, et al. (2003) Raman spectroscopy study of β-irradiated silica glass. *J Non-Cryst Solids* 325: 22–28. https://doi.org/10.1016/S0022-3093(03)00334-X
36. Galeener FL (1982) Planar rings in glasses. *Solid State Commun* 44: 1037–1040. https://doi.org/10.1016/0038-1098(82)90329-5
37. Darziyeva TA, Alekperov ES, Jabarov SH, et al. (2021) Vibrational properties of nanoparticles iron oxide by Raman spectroscopy. *Mod Phys Lett B* 35: 2150125. https://doi.org/10.1142/S0217984921501256
38. Zoppi A, Lofrumento C, Castellucci EM, et al. (2008) Al-for-Fe substitution in hematite: The effect of low Al concentrations in the Raman spectrum of Fe_2O_3. *J Raman Spectrosc* 39: 40–46. https://doi.org/10.1002/jrs.1811
39. Bost N, Duraipandian S, Guimbretière G, et al. (2016) Raman spectra of synthetic and natural mullite. *Vib Spectrosc* 82: 50–52. https://doi.org/10.1016/j.vibspec.2015.11.003
40. Bates JB (1972) Raman spectra of α and β cristobalite. *J Chem Phys* 57: 4042–4047. https://doi.org/10.1063/1.1678878
41. Trukhin A, Smits K, Chikvaidze G, et al. (2011) Luminescence of silicon dioxide—Silica glass, α-quartz and stishovite. *Cent Eur J Phys* 9: 1106–1113. https://doi.org/10.2478/s11534-011-0016-5
42. Pathak N, Gupta SK, Sanyal K, et al. (2014) Photoluminescence and EPR studies on Fe^{3+} doped $ZnAl_2O_4$: An evidence for local site swapping of Fe^{3+} and formation of inverse and normal phase. *Dalton Trans 43:* 9313–9323. https://doi.org/10.1039/C4DT00741G
43. Cannas M (2002) Luminescence properties of point defects in silica. *arXiv*. https://doi.org/10.48550/arXiv.cond-mat/0203284

44. Patel N, Mariazzi S, Toniutti L, et al. (2007) Structural evolution of nanoporous silica thin films studied by positron annihilation spectroscopy and Fourier transform infrared spectroscopy. *J Phys App Phys* 40: 5266. https://doi.org/10.1088/0022-3727/40/17/038
45. Kalampounias AG, Yannopoulos SN, Papatheodorou GN (2006) Temperature-induced structural changes in glassy, supercooled, and molten silica from 77 to 2150 K. *J Chem Phys* 124: 014504. https://doi.org/10.1063/1.2136878
46. Ando MF, Benzine O, Pan Z, et al. (2018) Boson peak, heterogeneity and intermediate-range order in binary SiO_2–Al_2O_3 glasses. *Sci Rep* 8: 5394. https://doi.org/10.1038/s41598-018-23574-1
47. Morrow BA, Cody IA (1976) Infrared studies of reactions on oxide surfaces. 6. Active sites on dehydroxylated silica for the chemisorption of ammonia and water. *J Phys Chem* 80*:* 1998–2004. https://doi.org/10.1021/j100559a010
48. Ceresoli D, Bernasconi M, Iarlori S, et al. (2000) Two-membered silicon rings on the dehydroxylated surface of silica. *Phys Rev Lett* 84: 3887–3890. https://doi.org/10.1103/PhysRevLett.84.3887
49. Brinker CJ, Brow RK, Tallant DR, et al. (1990) Surface structure and chemistry of high surface area silica gels. *J Non-Cryst Solids* 120: 26–33. https://doi.org/10.1016/0022-3093(90)90187-Q
50. D'Souza AS, Pantano CG (2002) Hydroxylation and dehydroxylation behavior of silica glass fracture surfaces. *J Am Ceram Soc* 85: 1499–1504. https://doi.org/10.1111/j.1151-2916.2002.tb00303.x
51. Zachariasen WH (1932) The atomic arrangement in glass. *J Am Chem Soc* 54: 3841–3851. https://doi.org/10.1021/ja01349a006
52. Altemose VO (1961) Helium diffusion through glass. *J Appl Phys* 32: 1309–1316. https://doi.org/10.1063/1.1736226
53. Leiby CC, Chen CL (1960) Diffusion coefficients, solubilities, and permeabilities for He, Ne, H_2, and N_2 in Vycor glass. *J Appl Phys* 31: 268–274. https://doi.org/10.1063/1.1735556
54. T'Sai LS, Hogness TR (1932) The diffusion of gases through fused quartz. *J Phys Chem* 36: 2595–2600. https://doi.org/10.1021/j150340a007
55. Norton FJ (1953) Helium diffusion through glass. *J Am Ceram Soc* 36: 90–96. https://doi.org/10.1111/j.1151-2916.1953.tb12843.x
56. Borjigin H, Stevens KA, Liu R (2015) Synthesis and characterization of polybenzimidazoles derived from tetraaminodiphenylsulfone for high temperature gas separation membranes. *Polymer* 71: 135–142. https://doi.org/10.1016/j.polymer.2015.06.021
57. Zhao Z, Ma X, Li Z, et al. (2011) Synthesis, characterization and gas transport properties of MOF-5 membranes. *J Membr Sci* 382: 82–90. https://doi.org/10.1016/j.memsci.2011.07.048
58. Au LTY, Yeung KL (2001) An investigation of the relationship between microstructure and permeation properties of ZSM-5 membranes. *J Membr Sci* 194: 33–55. https://doi.org/10.1016/S0376-7388(01)00489-6

AIMS Press

© 2026 the Author(s), licensee AIMS Press. This is an open access article distributed under the terms of the Creative Commons Attribution License (https://creativecommons.org/licenses/by/4.0)